Effects of free heave motion on wave resonance inside a narrow gap between two boxes under wave actions

Junliang Gao[1, 2], Zhiwei He[1], Xianghong Huang[3 *], Qian Liu[1], Jun Zang[2], Gang Wang[4]

1. School of Naval Architecture and Ocean Engineering, Jiangsu University of Science and Technology, Zhenjiang 212100, China

2. Research Unit for Water, Environment and Infrastructure Resilience (WEIR), Department of Architecture and Civil Engineering, University of Bath, BA2 7AY, U.K.

3. College of Shipbuilding Engineering, Harbin Engineering University, Harbin, 150001, China

4. College of Harbour, Coastal and Offshore Engineering, Hohai University, Nanjing 210098, China

Abstract: Fluid resonance inside a narrow gap between two side-by-side boxes is investigated based on an open-source CFD package, OpenFOAM. An upstream box heaves freely under wave actions and a downstream box remains fixed. The focus of this work is to study the influence of the motion of the upstream box on the hydrodynamic behavior of the resonant fluid inside the gap. The hydrodynamic behavior considered in this study includes the wave height inside the gap, heave displacement and their harmonic components, and reflection, transmission and energy loss coefficients. For comparison, the configuration in which the two boxes are fixed is considered. It was found that the heave motion of the upstream box increases the fluid resonant frequency and significantly reduces the resonant wave height in the gap. The frequencies at which the maximum and minimum heave displacements of the upstream box are observed to obviously deviate from the fluid resonant frequency. For the wave height in the gap and heave displacement, the effects of the incident wave height on their harmonic components are different. The heave motion of the upstream box results in a larger reflection coefficient and smaller energy loss coefficient.

Keywords: Gap resonance; Wave height amplification; Heave motion; Harmonic analysis; OpenFOAM

[*] Corresponding author. E-mail: xianghonghuang@qq.com

1. Introduction

Recently, as offshore oil and gas operations have advanced towards deeper water and harsher environments, floating production storage and offloading (FPSO) and floating liquefied natural gas (FLNG) production systems have been widely used in ocean engineering. For offloading operations from FPSO or FLNG to shuttle tanks, a key hydrodynamic issue lies in the occurrence of fluid resonance in the narrow gap between them under wave actions. The close proximity of the side-by-side marine structures can generate drastic water surface oscillations at certain frequencies in the narrow gap under wave actions, which lead to violent variations of hydrodynamic forces on the structures. This phenomenon is referred to as "gap resonance". In fact, similar resonance phenomena of the semi-enclosed water body with various spatial scales are common in the field of coastal and offshore engineering, such as harbor resonance (Gao et al., 2019c, 2020c) and moonpool resonance (Huang et al. 2020a, b).

The gap resonance phenomenon between multiple bodies has been investigated extensively. Early studies focused on theoretical analyses and were mainly based on the linear potential theory (Miao et al., 2001; Molin, 2001). Subsequently, to better understand the gap resonance and validate the theoretical analyses, certain laboratory experiments were conducted. Saitoh et al. (2006) conducted a series of two-dimensional experiment tests in a wave flume to investigate the gap resonance and found that the resonant wave height inside the narrow gap is dependent on the body draft and gap breadth. This finding proved the analytical results of Molin (2001). Iwata et al. (2007) extended this work to the three-body problem and their studies indicated that the resonance phenomenon was significantly affected by the number of boxes. Ning et al. (2018) experimentally studied the fluid resonance in the gap between two barges of different draughts in a wave flume and confirmed that an increase in either barge draught would lead to a decrease in the fluid resonant frequency. Recently, certain three-dimensional physical tests have been conducted (Zhao et al., 2017).

Previous studies demonstrated that the potential flow theory can predict the resonance frequencies and capture resonant modes. However, the resonant wave height was reported to be over-predicted when compared with the experimental results because the potential flow theory fails to consider the energy dissipation caused by the fluid viscosity, vortex shedding, and turbulence. To overcome this problem, several numerical techniques, such as introducing an artificial damping term in the linear potential flow theory, were developed for the over-predicted resonant wave height to be consistent with that of the experimental results (Chen, 2004; Newman, 2004; Ning et al., 2015; Tan et al., 2019). However, the artificial damping coefficient must be determined using physical experiments or computational fluid dynamics (CFD) simulations (Lu et al., 2011a, b). For the same structures and incident waves, different values of the artificial damping coefficient may be required for different physical quantities, such as wave forces on structures and wave heights in narrow gaps (Tan et al. 2014; Pauw et al. 2007).

Recently, with the rapid development of computing and numerical technology, the CFD simulation has emerged as an alternative method to study the gap resonance problem. Using a two-dimensional viscous numerical wave flume based on the Navier–Stokes equations and Clear-VOF technique, Lu et al. (2011a) investigated the fluid resonance in two fixed boxes with a gap and three fixed boxes with two gaps in between them. Based on an open-source CFD package, OpenFOAM, Moradi et al. (2015) systematically studied the influences of inlet configurations on the fluid resonance in the gap between two fixed bodies. Gao et al. (2019b) and Gao et al. (2020a) adopted the OpenFOAM to study the gap resonance between two fixed boxes induced by regular waves and focused wave groups, respectively. Gao et al. (2019a) and Gao et al. (2020b) investigated the resonant wave height inside the gap and wave forces in gap resonance between the fixed box and vertical wall, respectively. These investigations found that the numerical results predicted by the CFD simulations corresponded well with the existed experimental data.

Although numerous studies have investigated the gap resonance, most studies have assumed that the structures are fixed in the wave flume (Feng et al., 2017; Gao et al., 2019a, 2020b; Gao et al., 2019b; Jiang et al., 2019; Jiang et al., 2018; Lu et al., 2011a; Lu et al., 2011b; Ning et al., 2018; Sun et al., 2010; Zhao et al., 2018). However, in practical engineering situations, marine structures are not fixed but have a certain degree of freedom. For example, a shuttle tank may heave on the sea during offloading operations under wave actions. Here, previous studies on the fluid resonance between two fixed boxes may not be applicable to floating structures because the latter moves under wave actions. To date, quite few studies on gap resonance have considered floating structures with a certain degree of freedom of motion (Li, 2019; Li and Zhang, 2016). However, in these studies, the potential flow method is used and its defects have not been overcome. It is unknown whether the results correspond with the practical situations. To the best of the authors' knowledge, the simultaneous and synchronous motion of two structures was primarily considered in previous studies, and studies that considered solely the motion of a single box have not been found. Thus, to understand the influence of free heave motion of an upstream box on gap resonance, this study focuses on the gap resonance formed inside a two-box system where the upstream box heaves freely and the downstream box remains fixed.

The remainder of this paper is organized as follows: Sections 2 and 3 introduce the numerical model employed in this work and numerical wave tank setup, respectively. The validations of the numerical model are presented in Section 4. The numerical results and discussions are presented in Section 5. Finally, the conclusions are presented in Section 6.

2. Description of numerical model

A viscous flow solver is required to consider the physical energy dissipation near the gap due to the viscous effect. In this study, the viscous numerical wave flume is based on OpenFOAM, and the multiphase flow solver for dynamic mesh, *waveDyMFoam*, is selected. Regular waves are generated and absorbed using the relaxation-based wave generation toolbox *waves2Foam* proposed by Jacobsen et al. (2012).

2.1. Governing equations

The multiphase flow solvers, *waveDyMFoam*, use the Navier–Stokes equations to describe the motion of the fluid continuum. These equations can be expressed as:

$$\frac{\partial \rho}{\partial t} + \nabla \cdot (\rho \vec{U}) = 0 \qquad (1)$$

$$\frac{\partial \rho \vec{U}}{\partial t} + \nabla \cdot (\rho \vec{U}\vec{U}) - \nabla \cdot (\mu \nabla \vec{U}) - \rho \vec{g} = -\nabla p - \vec{f_\sigma} \qquad (2)$$

where $\vec{U}$ is the flow velocity vector, ρ is the density of the fluid, μ is the dynamic viscosity, $\vec{g}$ is the acceleration due to gravity, p is the pressure of the fluid, and $\vec{f_\sigma}$ is the surface tension.

To track the shape and position of the free surface, the volume of fluid (VOF) method has been employed in OpenFOAM. In grid cells, the volume fraction used in the VOF method is defined as follows:

$$\gamma = \begin{cases} 0, & \text{in air} \\ 0 < \gamma < 1, & \text{on the surface} \\ 1, & \text{in water} \end{cases} \tag{3}$$

The velocity field can be obtained using the weighted averages using the equation $\vec{U} = \gamma \vec{U}_{water} + (1-\gamma)\vec{U}_{air}$. According to this equation of the velocity field, the transport equation of the VOF field can be expressed as:

$$\frac{\partial \gamma}{\partial t} + \nabla \cdot (\gamma \vec{U}) + \nabla \cdot [\gamma (1-\gamma) \vec{U}_r] = 0 \tag{4}$$

where $\vec{U}_{water}$ and $\vec{U}_{air}$ are the velocities of the corresponding water and air, respectively. $\vec{U}_r = \vec{U}_{water} - \vec{U}_{air}$ indicates the relative velocity between air and water.

The spatial variation of any fluid property ϕ (e.g., the fluid density ρ and dynamic viscosity μ) can be expressed as weighting using γ:

$$\phi = \gamma \phi_{water} + (1-\gamma)\phi_{air} \tag{5}$$

where the subscripts “water” and “air” denote the corresponding fluid property of water and air, respectively.

2.2. Body motion equations

In this study, the motion of the floating body is restricted to one degree of freedom, allowing solely the heave motion (z-direction). The vertical position of the floating box is solved using Newton's second law at the current time step n+1:

$$F^{n+1} = ma^{n+1} \tag{6}$$

where F^{n+1} is the total vertical force (including gravity) calculated by integrating the pressure and shear forces acting on the body’s surface, and a^{n+1} is the body’s vertical acceleration. Once the acceleration a^{n+1} is known, the vertical velocity v^{n+1} and vertical position z^{n+1} at the current time step n+1 are calculated using an integration strategy:

$$v^{n+1} = v^{n+1} + (1-\theta)a^n \Delta T + \theta a^{n+1} \Delta T \tag{7}$$

$$z^{n+1} = z^n + (1-\theta)v^n \Delta T + \theta v^{n+1} \Delta T \tag{8}$$

where n is the previous time step, ΔT is the time step, and θ is a blending parameter. For $\theta = 0$, the forward Euler method, which is explicit in time arises, and for $\theta = 1$, the backward Euler method, which is fully implicit in time, are employed.

2.3. Mesh motion

The mesh motion of the computational domain is calculated by solving the cell-center Laplace smoothing equation (Jasak and Tukovic, 2006):

$$\nabla \bullet (\kappa \nabla \boldsymbol{u}) = 0 \tag{9}$$

where κ is the diffusion field and $\boldsymbol{u}$ is the point velocity for modifying the point position of the mesh:

$$\boldsymbol{x}^{n+1} = \boldsymbol{x}^{n} + \boldsymbol{u} \cdot \Delta T \tag{10}$$

where $\boldsymbol{x}^{n}$ and $\boldsymbol{x}^{n+1}$ are the point positions before and after mesh motion, respectively, and ΔT is the time step.

Using the variable diffusion field κ, the deformation of each grid point is scaled from the total body displacement to no deformation. Further, κ is a function of the distance r between the center of the cell and nearest selected boundary, where $r \in (r_i, r_o)$. r_i and r_o are the inner and outer distances of the scaling, respectively. The details of the diffusion method and several sub-options can be found in OpenFOAM User's Guide (Greenshields, 2015). In this study, the distance-based quadratic method was selected. The diffusivity of the field is based on the inverse of the distance from the selected boundary, and the variable diffusion field equals $1/r^2$.

2.4. Boundary conditions and numerical implementations

The relaxation-based toolbox *waveDyMFoam* developed by Jacobsen et al. (2015) was used to generate and absorb waves at the boundaries (see Fig. 1). For the inlet and outlet boundaries, the velocity was set as the incident wave velocity and zero, respectively, and the pressure gradients were set to zero. To absorb the reflected and transmitted waves, relaxation zones were provided at the inlet and outlet boundaries. The velocity boundary condition of the floating box is defined as *movingWallVelocity*.

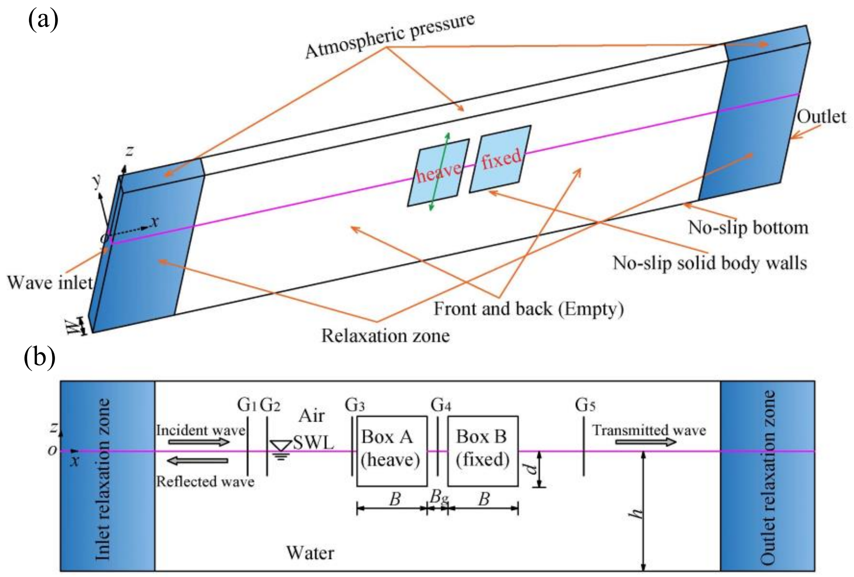

Fig. 1. Sketch of the numerical flume: (a) boundary conditions and the coordinate system; (b) positions of wave gauges and the definition of the geometric parameters

The finite volume method was used to solve the governing equations (1), (2), and the advection transport equation (3). The velocity−pressure coupling is resolved using the PISO (pressure implicit with splitting of the operator) algorithm (Jasak, 1996). Gradients are approximated using the Gaussian integration method based on a linear interpolation from cell centers to cell faces. The displacement and velocity of the floating box are obtained by solving equations (7) and (8), and the grid position in the deformation domain is calculated according to the floating box position and diffusion field.

In the present numerical cases, the time step is automatically determined according to the Courant-Friedrichs-Lewy (CFL) condition,

$$\Delta t \le C_r \times \min\left\{ \sqrt{S_e} / |u_e| \right\}, \tag{11}$$

where S_e and $|u_e|$ are the area and absolute velocity in a computational cell, respectively. To produce accurate and stable results, the largest Courant number C_r was set to 0.25 in all simulations.

3. Numerical wave flume

Fig. 1 shows the two-dimensional numerical wave flume used in this study. The numerical flume is 18.5 m long and 0.9 m high. According to the setting of the two-dimensional computational domain in OpenFOAM, the width of the numerical wave flume in this study is set as a grid cell with width W=0.02 m. The origin of the coordinate system is located at the static water level (SWL) of the left inlet boundary. The wave propagation direction is defined as the x-axis, and the upward direction is the z-axis. Two identical rectangular boxes were placed in the middle of the wave flume. The upstream and downstream boxes are Box A and Box B, respectively. The dimensions of the two boxes are: height H=0.5 m and breadth B=0.5 m, draft d=0.25 m, gap width B_g=0.05 m, and water depth h=0.5 m. And the density of boxes is 500 kg/m^3. This configuration is similar to the numerical investigations reported by Lu et al. (2011a) and physical experimental tests conducted by Saitoh et al. (2006). Two series of numerical experiments were conducted to compare the effects of upstream box motion on gap resonance. In the first series, the two boxes are fixed in the wave flume. In the second series, Box A heaves freely under incident wave actions, while Box B remains fixed. For simplicity, in the following description, the two-box system in the first series is called "*fixed structure system*" and that in the second series is called "*heave structure system*".

Five groups of incident wave heights were numerically simulated, where the wave heights of regular incident waves were set as H_0=0.01 m, 0.02 m, 0.03 m, 0.04 m, and 0.05 m, respectively. The wave frequency, ω, which was considered in all the simulations, ranges from 4.456 rad/s to 6.323 rad/s. According to the linear dispersion relation:

$$\omega^2 = gk\tanh(kh) \tag{12}$$

the dimensionless wavenumber, kh, ranges from 1.21 to 2.10, where $k = 2\pi / L$ denotes the wavenumber and L denotes the incident wavelength. Five wave gauges, G_1−G_5, as shown in Fig. 1, were used to record the wave elevation. G_1 and G_2 were used to separate the incident and reflected waves, and the distance between them was set to 0.25 m. G_3 and G_4 were used to obtain the free-surface elevation in front of Box A and wave elevation in the gap, respectively, and G_5 was used to record the transmission wave. G_4 was in the middle of the narrow gap, while G_2, G_3, and G_5 were situated at 1.5 m and 0.05 m from the left side of Box A and 1.5 m from the right side of Box B, respectively. Two relaxation zones, whose lengths were 6.0 m, were arranged on the inlet and outlet boundaries to absorb the reflection and transmission waves, respectively. The length of 6 m is about twice the maximum wavelength of the incident regular wave.

The built-in mesh generation utility provided by OpenFOAM, *blockMesh*, was used to generate meshes. Fig. 2 shows a typical computational mesh. Non-uniform meshes were adopted to save computational time. Fine meshes with higher resolution were employed around the boxes, particularly in the vicinity of the narrow gap. To accurately capture the motion of the free surface, the mesh density was gradually increased from the atmosphere and bottom boundary to the still water level.

Table 1. Details of coarse, middle, and fine meshes

Mesh	No. of cells	No. of points	No. of faces	Size of cells across the gap (m)	
				Δx	Δz
Coarse	136520	275602	547362	0.0042	0.0025
Middle	211960	426970	849366	0.0031	0.0020
Fine	317400	638338	1271370	0.0025	0.0016

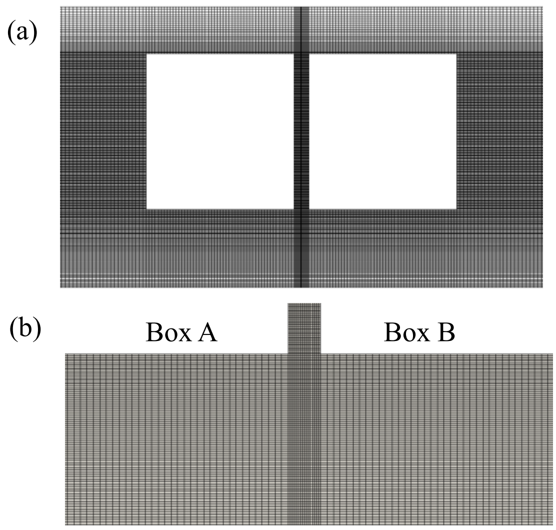

Fig. 2. Side view of typical meshes in the computational domain: (a) the meshes around the boxes; (b) the meshes close to the gap inlet

The mesh dependency is examined using three different meshes, viz., coarse, middle, and fine meshes. The details of the three different meshes are listed in Table 1. Based on the numerical results presented in Section 5.1, for the fixed structure system subjected to incident waves with H_0=0.01 m, the free-surface resonance inside the gap occurs at kh=1.556. For the heave structure system exposed to the same incident waves, the free-surface resonance occurs at kh=1.720. Fig. 3 presents the time histories of the free-surface elevation in the gap for the fixed and heave structure systems and the heave displacement of Box A excited by the incident waves with H_0=0.01 m. It can be observed that the time histories of the free-surface elevation inside the narrow gap and heave displacement of Box A exhibit very little discrepancy for the three meshes. In this study, the middle mesh was adopted in all numerical experiments.

The total simulation time is 40.0 s for the fixed structure system and 50.0 s for the heave structure system. It can be seen from Fig. 3 that the free-surface elevation in the gap for the fixed structure system has reached a steady state at t=20.0 s, and the free-surface elevation in the gap and heave displacement for the heave structure system reached a steady state at t=30.0 s. All the numerical results in Section 4 and Section 5 are based on the simulated steady state results from 20.0−40.0 s for the fixed structure system and 30.0−50.0 s for the heave structure system.

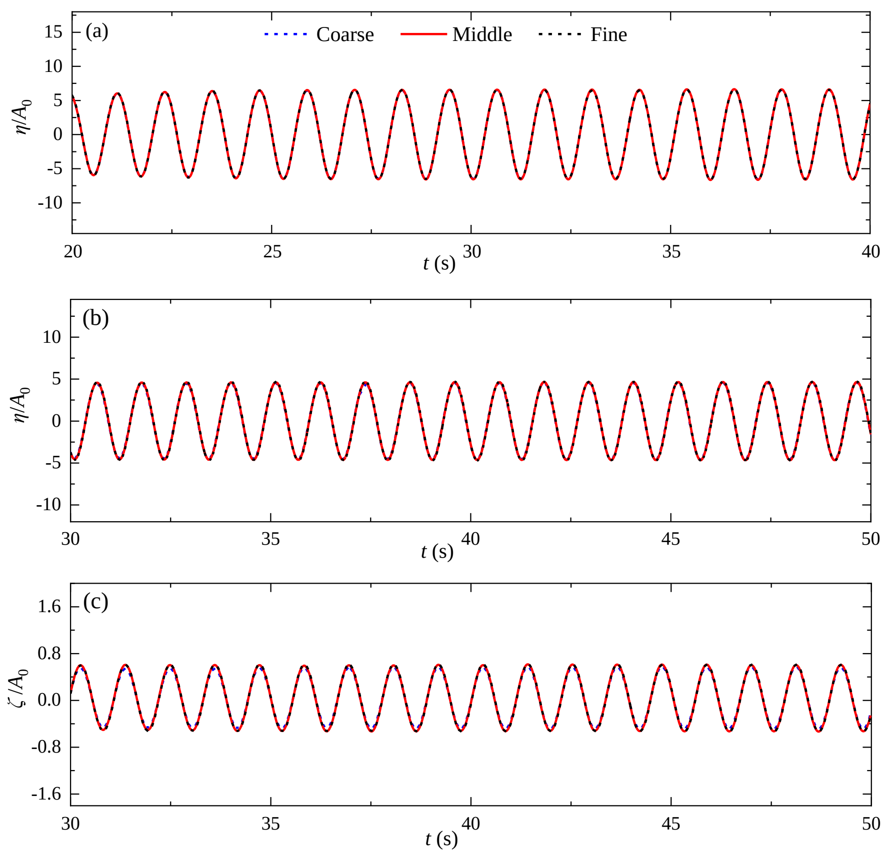

Fig. 3. Dependence of the free surface elevation in the gap and heave displacement of Box A on the mesh resolution. (a) the free surface elevation inside the narrow gap induced by the incident waves with kh=1.556, H_0=0.01 m for the fixed structure system. (b) and (c) the free surface elevation inside the narrow gap and heave displacement of Box A excited by incident waves with kh=1.720, H_0=0.01 m for the heave structure system, respectively. A_0=H_0/2 is the incident wave amplitude and ζ is the

heave displacement of Box A.

Using the same model mentioned above, a free decay test has been numerically performed for obtaining the natural period of the heave motion. The initial displacement of Box A is set to 0.01 m and then it heaves freely. Box B still keeps fixed. Fig. 4 shows the time history and the corresponding amplitude spectrum of the free decay of the heave motion of Box A. The natural frequency of the heave motion is about 0.6 Hz (equivalently, the natural wave number is $(kh)_N \approx 0.97$).

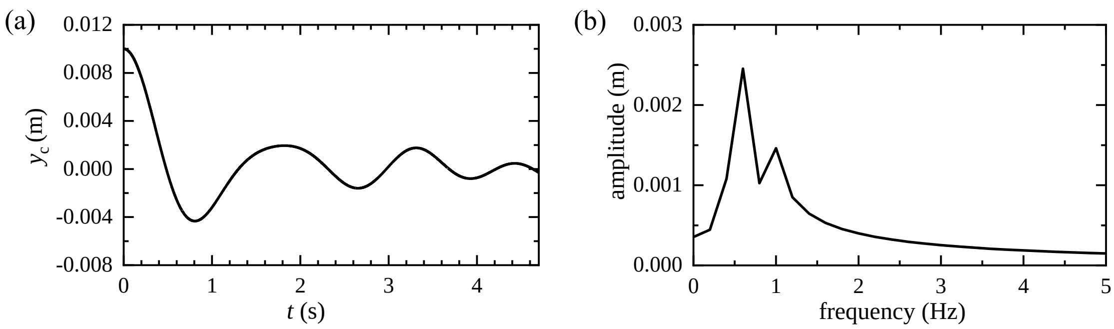

Fig. 4. (a) Time history and (b) corresponding amplitude spectrum of free decay of the heave motion of Box A.

4. Validation of numerical model

In this section, the previously mentioned numerical model and numerical wave flume are validated by comparing the simulation results of OpenFOAM with the available experimental data and numerical results presented in literature. Saitoh et al. (2006) and Lu et al. (2011b) studied the free-surface elevation in the narrow gap and wave forces on boxes using physical experiments and a viscous flow model, respectively. In Section 4.1, the numerical results of this study are compared with those of the two papers. However, their studies solely considered two fixed boxes. Because the free heave motion of Box A is allowed in the current study, the accuracy of the numerical model in simulating the motion of the structure should be further verified. Rodríguez and Spinneken (2016) measured the free heave motion of a single box under wave actions in the laboratory. A comparison between the present numerical results and their experimental data is presented in Section 4.2.

4.1. Verification of wave height amplification in the narrow gap

Fig. 5 shows the wave height amplification in the gap provided by the proposed numerical model, physical experimental, and viscous flow model where the wave height H_0=0.024 m. It can be seen that the proposed numerical model results correspond well with the experimental data measured by Saitoh et al. (2006) and viscous numerical solutions of Lu et al. (2011b). In addition, the resonant frequency predicted by the current numerical model is approximately equal to their results.

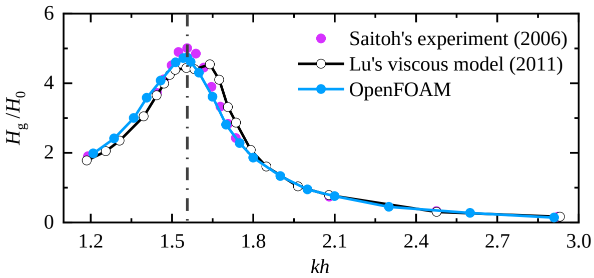

Fig. 5. Wave height amplification inside the narrow gap for the cases with H_0=0.024 m, where H_g denotes the wave height inside the narrow gap

4.2. Verification of the heave displacement of the box

Rodríguez and Spinneken (2016) conducted physical experiments in a wave tank of width=2.79 m, length=63 m, and water depth=1.25 m. The sketch of the wave tank used in the experiments is shown in Fig. 6. In the middle of the tank, a rectangular box is placed at x=29 m, where x=0 m is the position of the wavemaker. To satisfy the two-dimensional flow conditions, the width of the rectangular box was set to 2.76 m, such that the distance between the rectangular box and side walls of the tank is 0.015 m. Further dimensions of the box are breadth $2b$=0.5 m and draft d=0.25 m. Two steepness of the incident waves kA_0=0.05 and kA_0=0.10 are considered in the physical experiments. To examine the performance of the numerical model, a series of experiments with a steepness of kA_0=0.10 were conducted using OpenFOAM. Considering that the box used in the physical experiments has equal breadth and draft as those of the boxes in the numerical wave flume used in this study, the numerical wave tank, which is very similar to that in Fig. 1, is used for the present simulation (not reported in this paper for brevity). When compared with the wave flume shown in Fig. 1, two main differences are observed in the current wave flume. First, there is solely one box in the middle of the wave flume. Second, the water depth increases from 0.5 m to 1.25 m. A grid with a density similar to that of the middle mesh described in Section 3 is adopted. The length of the numerical wave flume need not be equal to that of the physical wave flume owing to the relaxation zone set at the inlet and outlet boundaries, and the length=18.5 m is sufficiently long.

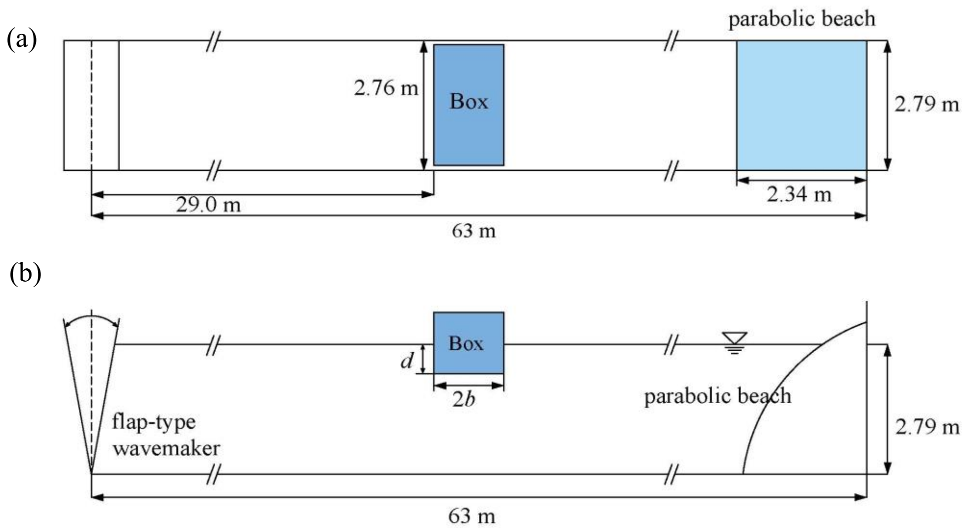

Fig. 6. Schematic of the wave flume setup of Rodríguez and Spinneken (2016): (a) plan view and (b) side elevation

Fig. 7 shows the comparison between the numerical simulation results, experimental data and linear potential flow prediction on the heave displacement. Rodríguez and Spinneken (2016) also obtained the linear potential flow prediction by solving the frequency-domain equation of motion using WAMIT. The results show that the numerical simulation results correspond well with those of the physical experiments, and the overall trend was sufficiently captured. When combined with the numerical simulation results of Sections 4.1 and 4.2, it can be confirmed that the current numerical model and numerical results are sufficiently reliable and accurate.

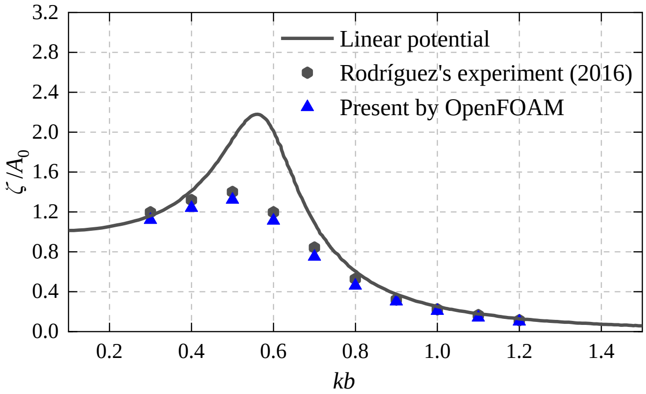

Fig. 7. Comparison of the heave displacement between the numerical and experimental results

5. Results and discussion

To understand the effect of the heave motion of Box A on the hydrodynamic characteristics of gap resonance, Section 5.1 discusses the variation of the overall wave height amplification inside the narrow gap with respect to the incident wave frequency for the fixed and heave structure systems. Then, to determine the relative importance of different harmonic components, Section 5.2 analyzes the first three harmonic components of the wave height amplification inside the narrow gap. Section 5.3 presents the variation of the heave displacement of Box A with respect to the incident wave frequency and attempts to understand the internal relationship between the heave motion of Box A and the characteristics of the free-surface resonance inside the gap. Subsequently, the harmonic analysis of the heave displacement of Box A is presented in Section 5.4. To better understand the similarities and differences in the gap resonant hydrodynamics for the fixed and heave structure systems, the transmission, reflection and energy loss coefficients for the two structure systems are discussed in Section 5.5.

5.1. Overall wave height amplifications

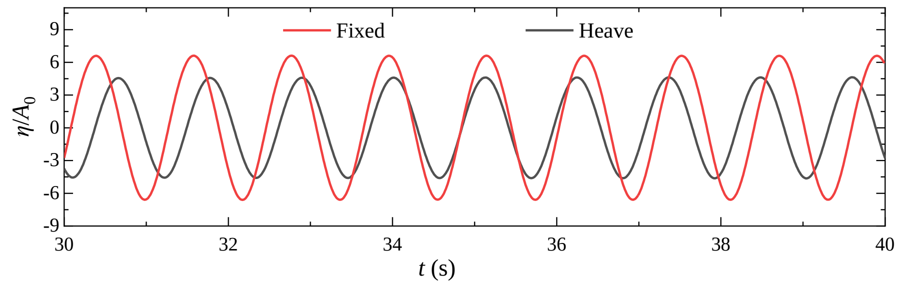

Fig. 8. Time histories of the free-surface elevation inside the gap for the fixed and heave structure systems under the condition that the fluid resonance occurs inside the gap excited by incident waves with H_0=0.01 m. For the fixed and heave structure systems, their fluid resonant frequencies are kh=1.556 and kh=1.720, respectively

Fig. 8 shows the time histories of the free-surface elevation inside the gap under the condition that the fluid resonance occurs inside the gap excited by incident waves with H_0=0.01 m. For the fixed and heave structure systems, their fluid resonant frequencies are kh=1.556 and kh=1.720, respectively, which can be seen from the following (i.e., Fig. 9). It can be observed from Fig.8 that the free-surface elevation in the gap of the heave structure system is smaller than that of the fixed structure system. It should be noted that the wave heights inside the gap, H_g, shown in Fig. 9 are computed using the averaged values of the simulated wave heights in the steady state between 20−40 s for the fixed structure system and 30−50 s for the heave structure system.

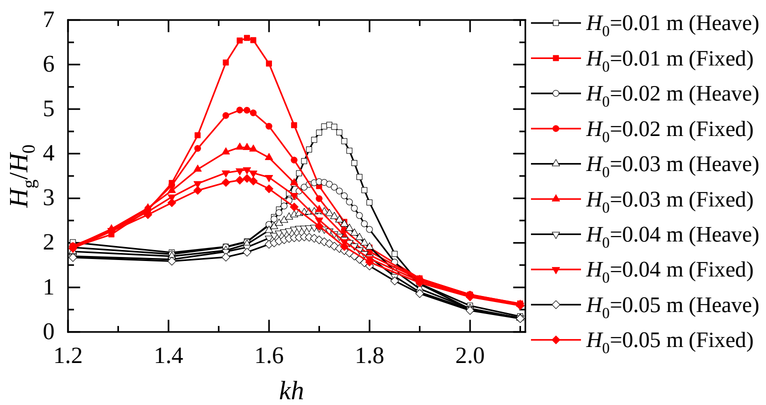

Fig. 9. Overall wave height amplification inside the gap for the fixed and heave structure systems excited by the incident waves with various wave heights

To further show the similarities and differences in the fluid resonant characteristics between the fixed and heave structure systems, Fig. 9 shows the wave height amplifications inside the gap for various incident wave heights. Three phenomena can be observed. First, for the two structure systems, the variation trend of wave height amplification with respect to the incident wave frequency is similar. The two trends show a single-peak shape. For a certain incident wave height, the maximum wave amplification occurs at a single fluid resonant frequency, and as the incident wave frequency deviates from the fluid resonant frequency, the wave height amplification gradually decreases. Second, for the fixed structure system, the fluid resonant frequency seems insensitivity to the incident wave height. For the heave structure system, it decreases with respect to the incident wave height. Fig. 10 further shows the variation of the fluid resonant frequency, $(kh)_{Hg}$, with respect to the incident wave height for the two structure systems, where the second phenomenon previously described can be seen more intuitively. Compare with the natural wave number ($(kh)_N \approx 0.97$), the fluid resonant frequencies of the heave structure system on various incident wave heights ($(kh)_{Hg}$=1.72–1.67) are higher.

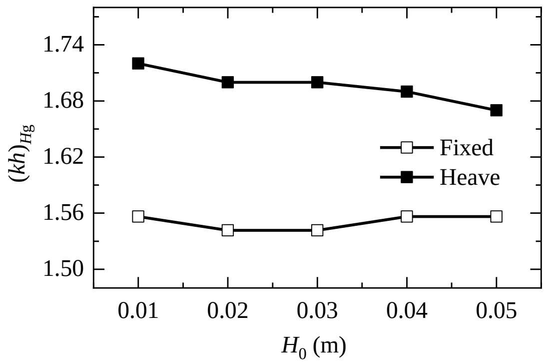

Fig. 10. Variation of fluid resonant frequency with respect to incident wave height for the two structure systems

Third, for the two structure systems, the wave height amplification inside the gap is affected by the incident wave height. To illustrate this phenomenon clearly, Fig. 11 further presents the variation of the resonant wave height, $(H_g/H_0)_{max}$, with respect to the incident wave height for the two structure systems. It can be observed that for the two structure systems, the maximum wave height amplification in the gap decreases continuously with an increase in the incident wave height. In addition, the value of $(H_g/H_0)_{max}$ for the fixed structure system is always larger than that for the heave structure system.

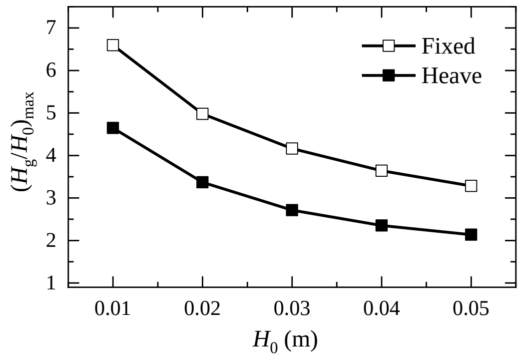

Fig. 11. Variation of the amplification of resonant wave height, $(H_g/H_0)_{max}$, with incident wave height for two structure systems

5.2. Harmonic analyses of wave height amplifications

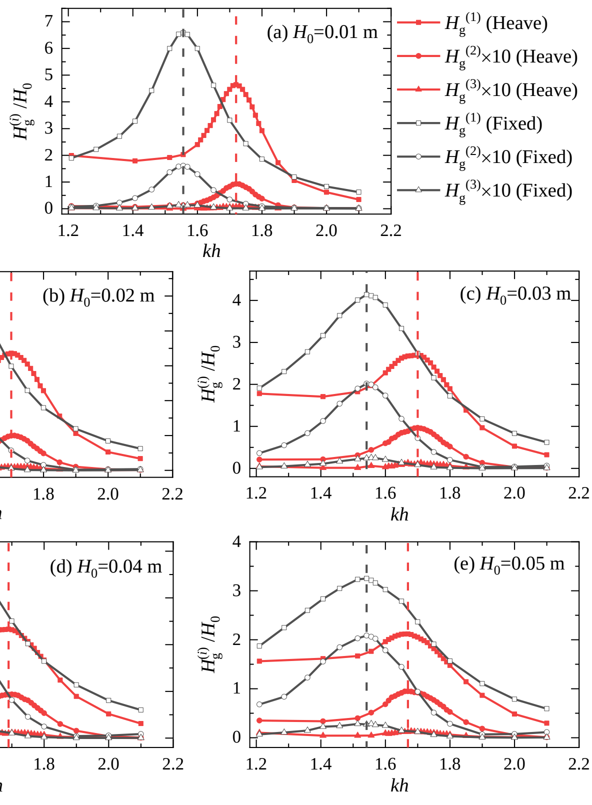

Fig. 12. First three order harmonic components of the wave height amplifications inside the gap under various incident wave heights. The black and red dashed lines represent the fluid resonant frequencies of the fixed and heave structure systems, respectively

Fig. 12 presents the first three order harmonic components of the wave height amplifications inside the gap under various incident wave heights for the two structure systems. $H_g^{(i)}$ (i=1, 2, and 3) in the figure denotes the i^{th}-order harmonic component of the wave height inside the gap. To clearly observe the high-order harmonic components, the second- and third-order components are magnified ten-fold. The following four phenomena can be observed. First, for the two structure systems, the first-order component of the wave height amplification is significantly larger than that of the corresponding second- and third-order components. Second, for the two structure systems, the first- and second-order harmonic components around the fluid resonant frequency are larger than the corresponding ones under non-resonant frequencies. As the incident wave height increases, this phenomenon can be observed for the third-order component. Third, the first- and second-order harmonic components around the fluid resonant frequency for the fixed structure system are larger than the corresponding ones for the heave structure system. This trend can be observed for the third-order component under larger incident wave heights. Fourth, the first-order harmonic component around the fluid resonant frequency decreases with an increase in the incident wave height. In addition, the difference between $H_g^{(1)}/H_0$ and the corresponding high-order values decreases with the incident wave height. The relative importance of the high-order components to the first-order component is analyzed further below.

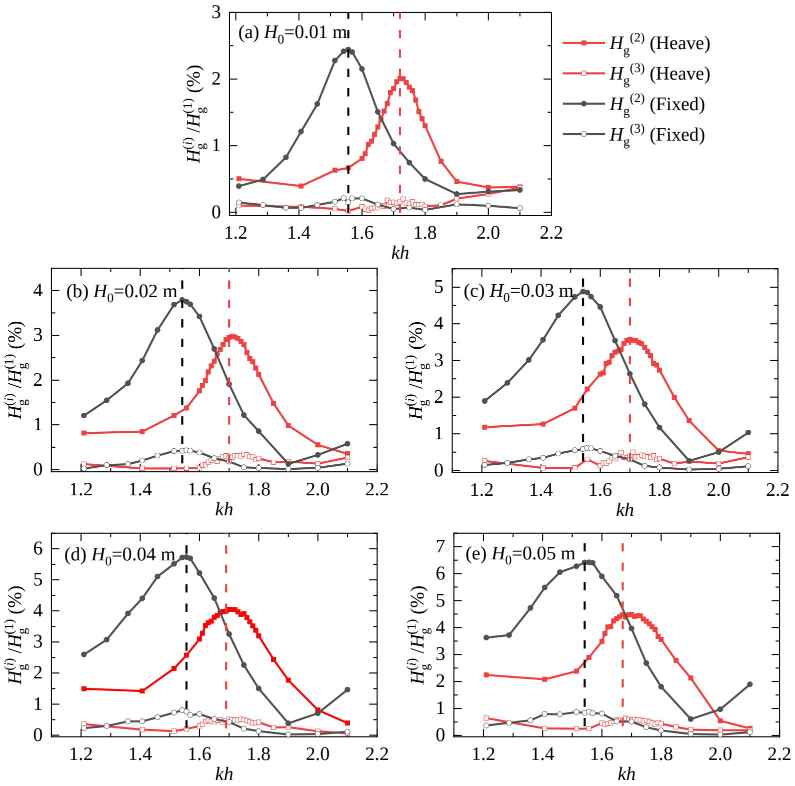

Fig. 13. Ratios of the second- and third-order harmonic components to the first-order ones under various incident wave frequency for the fixed and heave structure systems with different wave heights.

To quantify the relative importance of higher-order components to the first-order component, Fig. 13 further shows the ratios of the second- and third-order harmonic components to the corresponding first-order ones. The following three phenomena can be observed. First, for the fixed and heave structure systems, the ratios $H_g^{(2)}/H_g^{(1)}$ and $H_g^{(3)}/H_g^{(1)}$ around the fluid resonant frequency are significantly larger than the corresponding values for the non-resonant conditions, and their maximum occurs at or close to the fluid resonant frequency. Second, the ratios $H_g^{(2)}/H_g^{(1)}$ and $H_g^{(3)}/H_g^{(1)}$ at the fluid resonant frequency for the heave structure system are less than those for the fixed structure system. Third, Fig. 13 shows that the ratios $H_g^{(2)}/H_g^{(1)}$ and $H_g^{(3)}/H_g^{(1)}$ at the fluid resonant frequency increase with an increase in the incident wave height. To illustrate this phenomenon clearly, Fig. 14 illustrates the variations in the ratios $H_g^{(2)}/H_g^{(1)}$ and $H_g^{(3)}/H_g^{(1)}$ at the fluid resonant frequency with respect to the incident wave height. To illustrate the ratios $H_g^{(3)}/H_g^{(1)}$ clearly, they are magnified five times. The ratios $H_g^{(2)}/H_g^{(1)}$ and $H_g^{(3)}/H_g^{(1)}$ at the fluid resonant frequency for the fixed structure system increase significantly with an increase in incident wave height. For the heave structure systems, the ratios $H_g^{(2)}/H_g^{(1)}$ and $H_g^{(3)}/H_g^{(1)}$ at the resonant frequency increase with an increase in the incident wave height. However, their variation rates are lower than those of the fixed structure system. In addition, the ratios $H_g^{(2)}/H_g^{(1)}$ and $H_g^{(3)}/H_g^{(1)}$ at the resonant frequency for the fixed structure system are always larger than the corresponding values for the heave structure system.

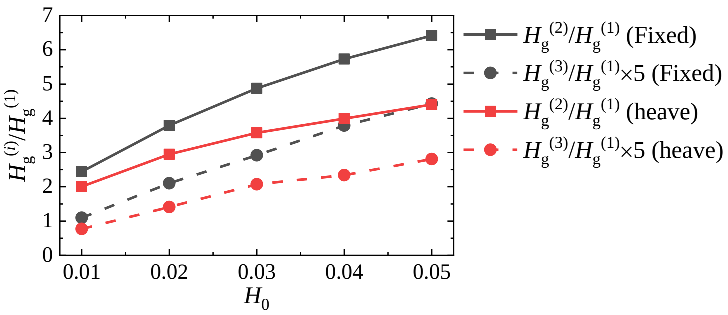

Fig. 14. Variations of the ratios $H_g^{(2)}/H_g^{(1)}$ and $H_g^{(3)}/H_g^{(1)}$ at the fluid resonant frequency with respect to the incident wave heights

5.3. Heave displacement of Box A

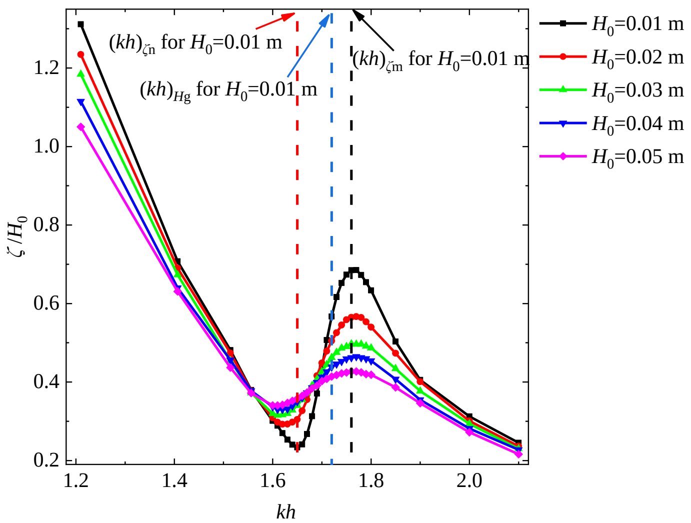

Fig. 15. Heave displacements of Box A excited by the incident regular waves with various wave heights, where $(kh)_{\zeta m}$ and $(kh)_{\zeta n}$ represent the incident wave frequencies at which the global maximum and minimum heave displacements occur for a certain incident wave height

Fig. 15 shows the heave displacements of Box A excited by the incident regular waves with various wave heights. The heave displacement ζ is normalized by the incident wave height H_0. Further, the incident wave frequencies at which the maximum and minimum of the normalized displacement occur for a certain incident wave height are defined as $(kh)_{\zeta m}$ and $(kh)_{\zeta n}$. The following four phenomena can be observed. First, the normalized displacements excited by regular waves with low frequencies (kh<1.4) are much larger than those with higher frequencies. The reasons for this phenomenon are as follows: If solely one box is placed in the middle of the wave flume, the theoretical heave displacement of the box under the action of low-frequency waves should be close to the wave height, i.e., $\zeta/H_0 \approx 1$. When two boxes are placed side-by-side in the wave flume, if the incident waves are completely reflected by the downstream box, theoretically, ζ/H_0 should be close to 2. However, because the downstream box is a truncated structure, a part of the incident wave energy is transmitted to the gap and behind the two-box system. Therefore, the normalized displacement cannot reach under incident waves with low frequencies.

Second, when the normalized wave number kh is approximately less than 1.62, the normalized displacement gradually decreases with an increase in the wave frequency. When the wave frequency is roughly in the range of 1.62<kh<1.76, the normalized displacement increases rapidly with an increase in wave frequency. When the wave frequency is in the high-frequency range of kh>1.76, the normalized displacement at all incident wave heights decreases with an increase in the wave frequency. It can be observed that the variation trend of the normalized displacement with the wave frequency is different from that of the wave height amplification in the gap presented in Fig. 8.

To understand the parameters that determine the movement of Box A, Fig. 16 shows the time history of the vertical force on the Box A and the heave displacement at three typical wave frequencies (kh=1.65, 1.72 and 1.76) for the incident wave height H_0=0.01 m, in which $F_v^A/(\rho g h A_0 W)$ is the memorialized vertical force of Box A. It can be observed from Fig. 16 that the heave displacement increases with the increase of the vertical force. Therefore, the vertical force on Box A has an important influence on the heave displacement.

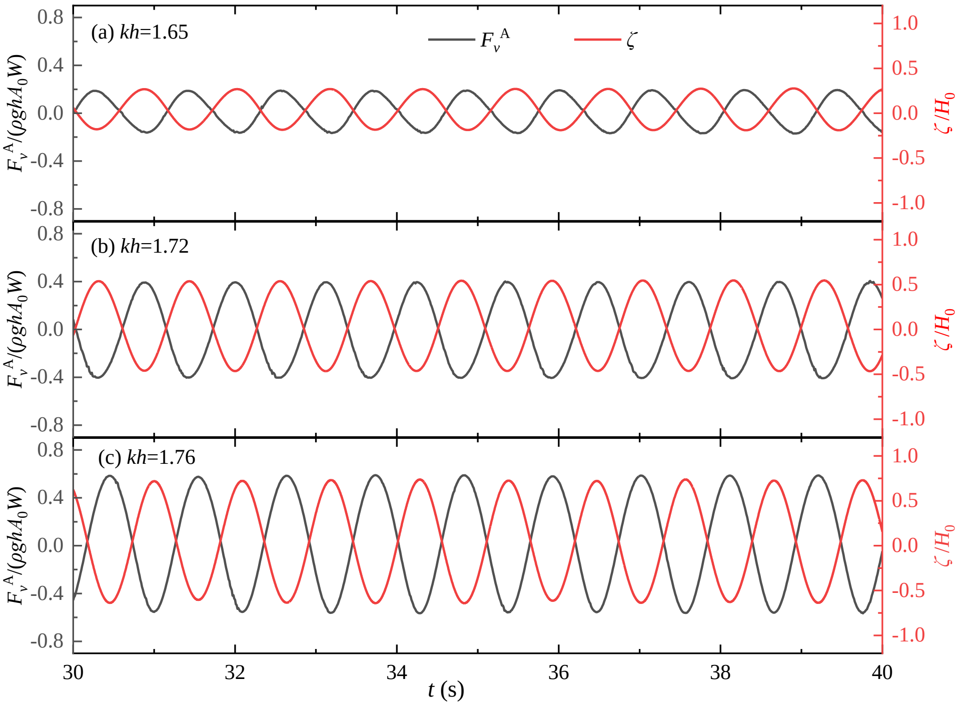

Fig. 16. Time history of the vertical force on the Box A and the heave displacement at three conventional wave frequencies (kh=1.65, 1.72 and 1.76) for the incident wave height H_0=0.01 m, in which $F_v^A/(\rho g h A_0 W)$ is the normalized vertical force of Box A

Third, by carefully observing the three frequencies of $(kh)_{Hg}$, $(kh)_{\zeta n}$, and $(kh)_{\zeta m}$ for each wave height in Fig. 15, it can be found that for all the incident wave heights considered, the frequencies of $(kh)_{\zeta m}$ and $(kh)_{\zeta n}$ are different from the corresponding fluid resonant frequencies $(kh)_{Hg}$. These values are greater and less than the corresponding $(kh)_{Hg}$ values respectively. To further illustrate the similarities and differences between $(kh)_{\zeta m}$, $(kh)_{\zeta n}$, and $(kh)_{Hg}$, their variations with the incident wave height are presented in Fig. 17. It can be observed that at the variation range of H_0 considered, the frequency $(kh)_{\zeta m}$ seems insensitivity to H_0, and slightly fluctuates at kh=1.760. The frequency $(kh)_{\zeta n}$ decreases continuously when H_0<0.03 m and remains constant when H_0>0.03 m. The fluid resonant frequency $(kh)_{Hg}$ presents a continuous decreasing trend for the entire variation range of H_0.

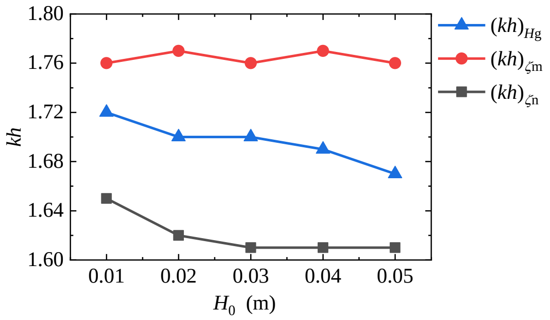

Fig. 17. Variations of the frequencies $(kh)_{\zeta\mathrm{m}}$, $(kh)_{\zeta\mathrm{n}}$ and $(kh)_{H\mathrm{g}}$ with the incident wave height

Forth, as the incident wave height increases, the maximum and minimum values of normalized heave displacements present a decreasing and increasing trend, respectively, and as the incident wave height increases, the difference between them gradually decreases. Fig. 18 further shows the variations of the normalized displacements excited by the incident waves with frequencies of $(kh)_{\zeta\mathrm{m}}$, $(kh)_{\zeta\mathrm{n}}$, and $(kh)_{H\mathrm{g}}$ with respect to the incident wave heights. The normalized displacement under the resonant frequency $(kh)_{H\mathrm{g}}$ continuously decreases with an increase in the incident wave height. Similar to the normalized displacement under the resonant frequency $(kh)_{H\mathrm{g}}$, the maximum normalized displacement decreases with an increase in the incident wave height. Similarly, the minimum of the normalized displacements continuously increases with an increase in the incident wave heights.

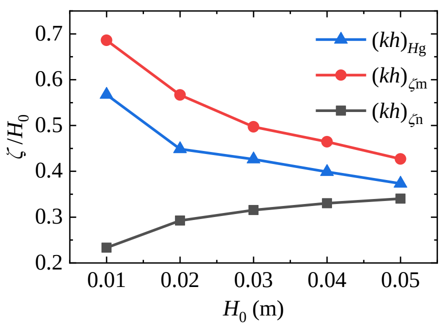

Fig. 18. Variations of the normalized displacement excited by wave frequencies of $(kh)_{\zeta\mathrm{m}}$, $(kh)_{\zeta\mathrm{n}}$, and $(kh)_{H\mathrm{g}}$

In addition, because the frequencies of $(kh)_{\zeta\mathrm{m}}$, $(kh)_{\zeta\mathrm{n}}$, and $(kh)_{H\mathrm{g}}$ are not equal to each other at each incident wave height, it can be seen from Fig. 9 that the wave height amplifications excited by these frequencies are different. Fig. 19 shows the variations in the wave height amplifications excited by wave frequencies of $(kh)_{\zeta m}$, $(kh)_{\zeta n}$, and $(kh)_{Hg}$ with incident wave height. It can be observed that the variation trends of H_g/H_0 for the frequencies $(kh)_{\zeta m}$, $(kh)_{\zeta n}$, and $(kh)_{Hg}$ are continuously decreasing with an increase in the incident wave height. However, their decreasing degrees are different. Among them, the decreasing degrees of the wave height amplification inside the narrow gap excited by wave frequencies of $(kh)_{\zeta m}$, $(kh)_{\zeta n}$, and $(kh)_{Hg}$ decreases gradually, but for the frequency of $(kh)_{\zeta n}$, the degree is smaller than other frequencies.

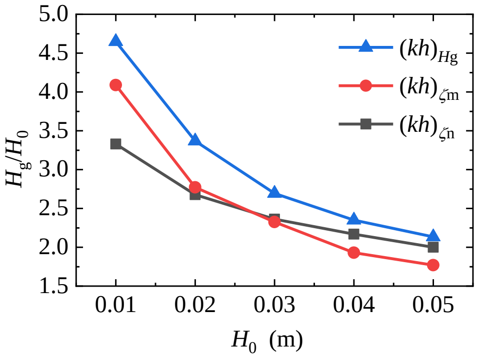

Fig. 19. Variations of the wave height amplifications inside the narrow gap excited by wave frequencies of $(kh)_{\zeta m}$, $(kh)_{\zeta n}$, and $(kh)_{Hg}$ with the incident wave height

5.4. Harmonic analyses of heave displacement

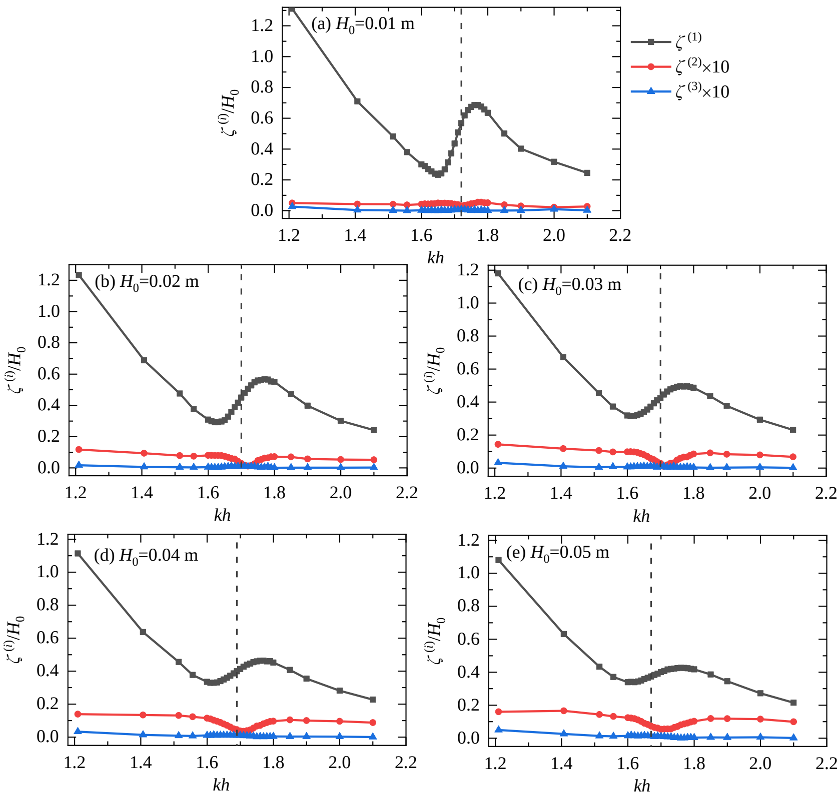

Fig. 20. First three harmonic components of the heave displacement under various incident wave heights, where the black dashed lines represent the fluid resonant frequency of the heave structure system

Fig. 20 shows the variation of the first three harmonic components of the heave displacement of Box A with respect to the incident wave frequency. In the figure, $\zeta^{(i)}$ (i=1, 2, and 3) represents the i^{th}-order harmonic component of the heave displacement. Similar to Fig. 12, to illustrate the high-order harmonic components clearly, their values are magnified ten-fold in this figure. The following three phenomena can be observed. First, the first-order harmonic component of the heave displacement is much larger than the corresponding high-order ones, and the latter are very small, as shown in Fig. 20, after the magnification. Moreover, the variation trend of the first-order component at each incident wave height first decreases, then increases, and then decreases. Second, the second-order components around the fluid resonant frequency are lower than the corresponding ones under non-resonant frequencies. Third, around the fluid resonant frequency, the third-order component of the heave displacement tends to approach or even exceed the corresponding second-order one.

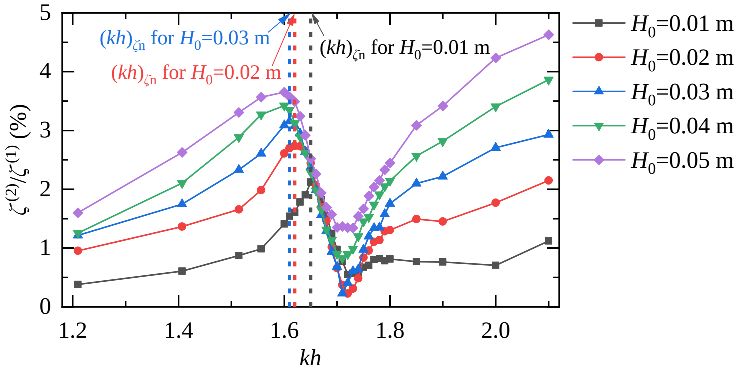

Fig. 21. Ratio of the second-order harmonic component of the heave displacement to the corresponding first-order one under various incident wave heights

To quantify the relative importance of the high-order components to the first-order component, Fig. 21 shows the ratio of the second-order harmonic component of the heave displacement to the corresponding first-order one. Considering that the magnitude of the third-order harmonic component is very small over the entire frequency range, its ratio to the corresponding first-order one is not discussed here. The following three phenomena can be observed. First, at $kh<1.62$ and $kh>1.71$, the ratio of the second-order component to the first-order component increases continuously with the wave frequency. In the range of $1.62<kh<1.71$, the ratio $\zeta^{(2)}/\zeta^{(1)}$ decreases sharply with the wave frequency. The value of $\zeta^{(2)}/\zeta^{(1)}$ for each wave height reaches the minimum value at or around the fluid resonant frequency, and the minimum value is between 0.2% and 1.5%. Second, generally, in the frequency range considered, the ratio $\zeta^{(2)}/\zeta^{(1)}$ increases with an increase in the incident wave height. For all cases, the maximum value of the ratio $\zeta^{(2)}/\zeta^{(1)}$ is 4.6% at kh=2.1, H_0=0.05 m. Third, for the relatively large wave heights (H_0=0.04 m and 0.05 m), the global maximum value of the ratio $\zeta^{(2)}/\zeta^{(1)}$ occurs at kh=2.1. For relatively small wave heights (H_0=0.01 m—0.03 m), the maximum value of the ratio $\zeta^{(2)}/\zeta^{(1)}$ occurs at or around the corresponding $(kh)_{\zeta n}$. In addition, there is a local maximum at frequency $(kh)_{\zeta n}$ for relatively large wave heights (H_0=0.04 m and 0.05 m).

5.5. Reflection, transmission and energy loss coefficients

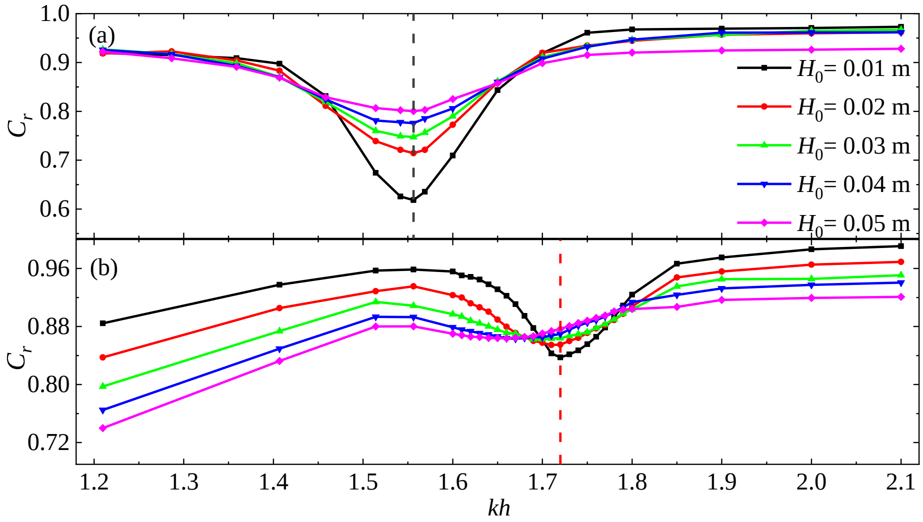

Fig. 22. Reflection coefficient, C_r, for (a) the fixed structure system, and (b) the heave structure system. The black and red dashed lines represent the fluid resonant frequency for the fixed and heave structure systems, respectively, under H_0=0.01 m.

Fig. 22 shows the reflection coefficient, C_r, for the two structure systems. It should be motioned that the reflected and transmitted waves considered in this section include the radiated waves generated by the heave motion of the Box A, and the radiated waves is theoretically impossible and unnecessary to be explicitly separated from the reflected and transmitted waves. The variation trend of the reflection coefficient for the fixed structure system is different from that for the heave structure system. For the fixed structure system, the reflection coefficient first decreases and then increases with an increase in the wave frequency. For the heave structure system, the reflection coefficient first increases, then decreases, and then increases. Besides, there is always a global minimum value (for the fixed structure system) or a local minimum value (for the heave structure system) of the reflection coefficient around the fluid resonant frequency. Another phenomenon is that for the two structure systems, the reflection coefficients at the fluid resonant frequency increase with an increase in the incident wave height, but the degree of increase for the heave structure system is not as clear as that of the fixed structure system.

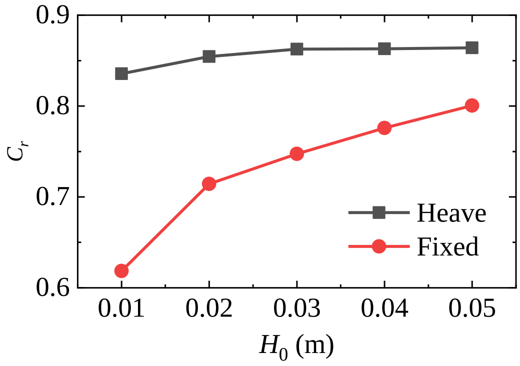

Fig. 23. Variations of the reflection coefficient at the resonant frequency for the two structure systems with the incident wave height

To better demonstrate the third phenomenon mentioned above, Fig. 23 shows the variations of the reflection coefficient at the fluid resonant frequency for the fixed and heave structure systems with respect to the incident wave height. The reflection coefficient for the fixed structure system at the resonant frequency increases significantly with an increase in the incident wave height. For the heave structure systems, the variation of C_r at the fluid resonant frequency increases with the incident wave height. However, its variation rate is lower than that of the fixed structure system. In addition, the reflection coefficients at the fluid resonant frequency for the heave structure system are always larger than those for the fixed structure. This may be because the radiation waves generated by the heave motion of Box A contribute to the reflection waves, resulting in a more significant reflection coefficient.

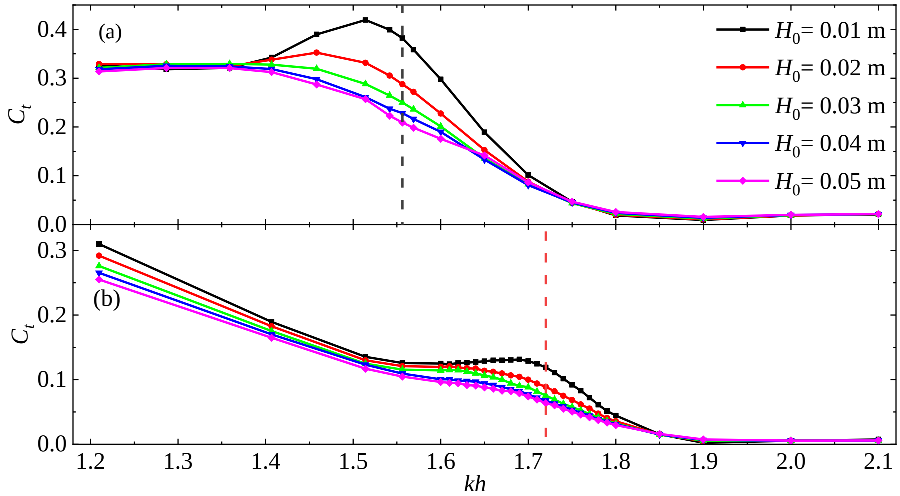

Fig. 24. Transmission coefficient, C_t, for (a) the fixed structure system, and (b) the heave structure system. The black and red dashed lines represent the fluid resonant frequency for the fixed and heave structure systems, respectively, under H_0=0.01 m.

Fig. 24 shows the transmission coefficient, C_t, for the fixed and heave structure systems. The following three phenomena can be observed: First, for the two structure systems, the frequency at which the maximum transmission coefficient occurs is smaller than the resonant frequency. Second, for the fixed structure system, when the incident wave height is small, the transmission coefficient first increases and then decreases with the wave frequency. With the increase in incident wave height, this trend gradually decreases continuously. For the heave structure system, the variation of the transmission coefficient is completely different from that of the fixed structure system. The transmission coefficient almost continuously decreases with the wave frequency at all the incident wave heights considered. Third, by comparing Figs. 22 and 24, it can be found that for the fixed and heave structure systems, the reflection coefficients are always larger than the transmission coefficients for all the incident wave heights considered in this study. The larger the incident wave height is a clear difference between C_r and C_t.

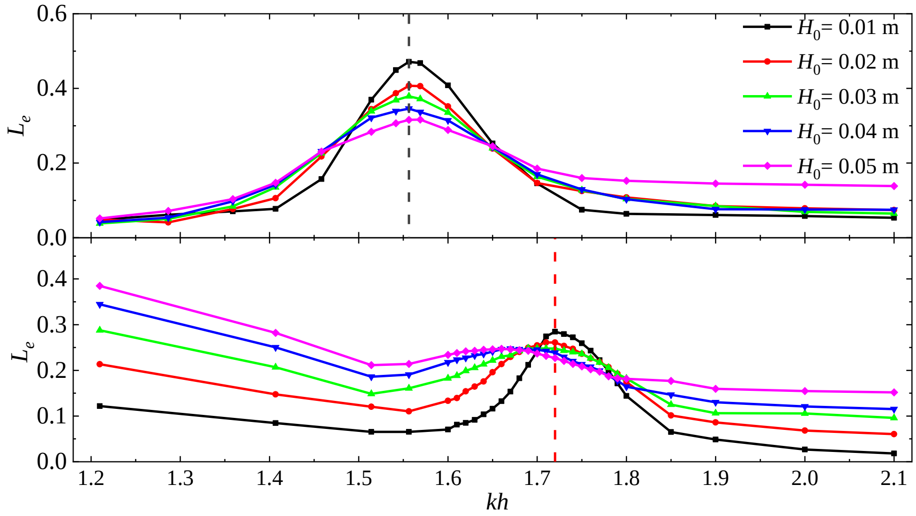

Fig. 25. Energy loss coefficient, L_e, for (a) the fixed structure system, and (b) the heave structure system. The black and red dashed lines represent the fluid resonant frequency for the fixed and heave structure systems, respectively, under H_0=0.01 m.

Fig.25 shows the energy loss coefficient, L_e, for the fixed and heave structure systems. The energy loss coefficient is formulated as $L_e = 1 - C_r^2 - C_t^2$. There is always a global maximum value (for the fixed structure system) or a local maximum value (for the heave structure system) of the energy loss coefficient around the fluid resonant frequency. Besides, the energy loss coefficients at resonant frequency for two structure systems decrease with the increase of the incident wave height. To clearly demonstrate this phenomenon, Fig. 26 shows the variations of the energy loss coefficient at the fluid resonant frequency for two structure systems. The energy loss coefficients at the fluid resonant frequencies for the heave structure system are always less than those for the fixed structure system, which indicates that the heave motion of upstream box will lead to less energy dissipation.

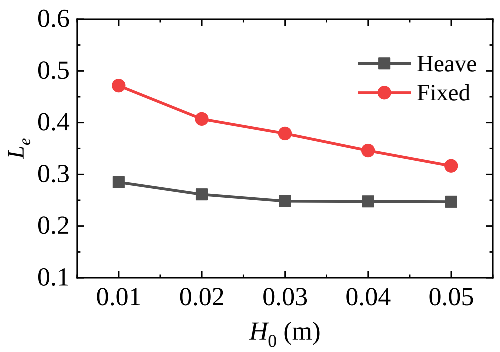

Fig. 26. Variations of the energy loss coefficient at the resonant frequency for the two structure systems with the incident wave height.

6. Conclusions

A two-dimensional numerical wave tank based on OpenFOAM was used to study the gap resonance formed between two boxes under the action of regular waves. In contrast to several previous studies on gap resonance where the structures were assumed to be fixed, the heave motion of the upstream box was considered in this study, and the influence of the motion of the box on the hydrodynamic behavior of the gap resonance are systematically investigated. Two series of numerical experiments were conducted to compare the effects of upstream box motion on gap resonance. In the first series, the two boxes are fixed in the wave flume. In the second series, Box A heaves freely under incident wave actions, while Box B remains fixed. The two-box system in the first series is called "*fixed structure system*" and that in the second series is called "*heave structure system.*" The variations of the wave height amplification in the gap with the incident wave height and wave frequency for the fixed and heave structure systems are compared. Subsequently, the harmonic components of the wave height amplification are analyzed. Then, the variation in the heave displacement of the upstream box with respect to the incident wave height and frequency, and its harmonic characteristics are investigated. Finally, the reflection, transmission and energy loss coefficients of the fixed and heave structure systems are discussed.

The following points summarize the results of this study:

(1) For the fixed and heave structure systems, the wave height amplification always increases first and then decreases with respect to the wave frequency. When compared with the fixed structure system, the heave motion of the upstream box leads to a lower wave height amplification inside the gap and a higher fluid resonant frequency, and this resonant frequency is very close to the natural frequency of the heave free decay. In addition, the fluid resonant frequency decreases significantly with an increase in the incident wave height for the heave structure system.

(2) For the fixed and heave structure systems, the first three harmonic components of the wave height inside the gap attain their respective peak values at or around the fluid resonant frequency. The ratios of the high-order components (including the second and third-order ones) to the corresponding first-order component near the resonant frequency are greater than those away from the resonant frequency. The ratios of the high-order components to the corresponding first-order component at the fluid resonant frequency for the fixed structure system are larger than those for the heave structure system.

(3) The heave displacement of the upstream box first decreases, then increases, and then decreases with an increase in the incident wave frequency. The maximum and minimum values of normalized heave displacements tend to decrease and increase with increasing incident wave height, respectively. The two frequencies at which the maximum and minimum displacements occur under each wave height deviate from the fluid resonant frequency obviously. Moreover, they are greater than and less than the fluid resonant frequency, respectively.

(4) The high-order components of the heave displacement of the upstream box are significantly small, and the third-order component of the heave displacement around the resonant frequency tends to approach or exceed the corresponding second-order component. The ratio of the second-order component to the corresponding first-order component under each wave height reaches the minimum value at or around the fluid resonant frequency. The global maximum value (for small incident waves having heights of 0.01−0.03 m) or local maximum value (for the larger incident waves having heights of 0.04 m and 0.05 m) of this ratio occurs at or around the corresponding frequency where the minimum displacement occurs.

(5) For all the incident wave heights considered in this study, the minimum reflection coefficient occurs at (or very close to) the resonant frequency for the two structure systems. The reflection coefficients at the fluid resonant frequency for the heave structure system are always larger than those for the fixed structure. The heave motion of upstream box will lead to less energy dissipation.

Acknowledgments

This research is financially supported by the National Key Research and Development Program (2017YFC1404200), the National Natural Science Foundation of China (Grant Nos. 51911530205), the Natural Science Foundation of Jiangsu Province (Grant No. BK20201455), the Natural Science Foundation of the Jiangsu Higher Education Institutions (Grant No. 20KJD170005) and the Qing Lan Project of Jiangsu Universities. The authors also thank UK EPSRC (Grant No. EP/R007519/1), the Royal Academy of Engineering (Grant No. UK-CIAPP/73) and the Royal Society (Grant No. IEC\NSFC\181321) for providing partial support for this work.

References

Chen, X.B., 2004. Hydrodynamics in Offshore and Naval Applications (Keynote lecture), The 6th International Conference on Hydrodynamics, Perth, Austrilia.

Feng, X., Bai, W., Chen, X.B., Qian, L., Ma, Z.H., 2017. Numerical investigation of viscous effects on the gap resonance between side-by-side barges. Ocean Engineering 145, 44-58.

Gao, J., Chen, H., Zang, J., Chen, L., Wang, G., Zhu, Y., 2020a. Numerical investigations of gap resonance excited by focused transient wave groups. Ocean Engineering 212, 107628.

Gao, J., He, Z., Zang, J., Chen, Q., Ding, H., Wang, G., 2019a. Topographic effects on wave resonance in the narrow gap between fixed box and vertical wall. Ocean Engineering 180, 97-107.

Gao, J., He, Z., Zang, J., Chen, Q., Ding, H., Wang, G., 2020b. Numerical investigations of wave loads on fixed box in front of vertical wall with a narrow gap under wave actions. Ocean Engineering 206, 107323.

Gao, J., Ma, X., Zang, J., Dong, G., Ma, X., Zhu, Y., Zhou, L., 2020c. Numerical investigation of harbor oscillations induced by focused transient wave groups. Coastal Engineering 158, 103670.

Gao, J., Zang, J., Chen, L., Chen, Q., Ding, H., Liu, Y., 2019b. On hydrodynamic characteristics of gap resonance between two fixed bodies in close proximity. Ocean Engineering 173, 28-44.

Gao, J., Zhou, X., Zhou, L., Zang, J., Chen, H., 2019c. Numerical investigation on effects of fringing reefs on low-frequency oscillations within a harbor. Ocean Engineering 172, 86-95.

Greenshields, C.J., 2015. OpenFOAM User Guide (Version 3.0.1). OpenFOAM Foundation Ltd.

Huang, X., Xiao, W., Yao, X., Gu, J., Jiang, Z., 2020a. An Experimental Investigation on Reduction Effect of Damping Devices for the Recessing Type Moonpool with a Large Aspect Ratio. Journal of Ship Research, 1-20.

Huang, X.H., Xiao, W., Yao, X.L., Gu, J.Y., Jiang, Z.Y., 2020b. An experimental investigation of reduction effect of damping devices in the rectangular moonpool. Ocean Engineering 196, 106767.

Iwata, H., Saitoh, T., Miao, G., 2007. Fluid resonance in narrow gaps of very large floating structure composed of rectangular modules, Proceedings of the 4th International Conference on Asian and Pacific Coasts, Nanjing, China, pp. 815-826.

Jacobsen, N.G., Fuhrman, D.R., Fredsøe, J., 2012. A wave generation toolbox for the open-source CFD library: OpenFoam®. International Journal for Numerical Methods in Fluids 70 (9), 1073-1088.

Jacobsen, N.G., Gent, M.R.A.v., Wolters, G., 2015. Numerical analysis of the interaction of irregular waves with two dimensional permeable coastal structures. Coastal Engineering 102, 13-29.

Jasak, H., 1996. Error Analysis and Estimation in the Finite Volume Method with Applications to Fluid Flows. PhD thesis, Imperial College, London.

Jasak, H., Tukovic, Z.J.T.o.F., 2006. Automatic mesh motion for the unstructured finite volume method. 30 (2), 1-20.

Jiang, S.-C., Bai, W., Cong, P.-W., Yan, B., 2019. Numerical investigation of wave forces on two side-by-side non-identical boxes in close proximity under wave actions. Marine Structures 63, 16-44.

Jiang, S.-C., Bai, W., Tang, G.-Q., 2018. Numerical simulation of wave resonance in the narrow gap between two non-identical boxes. Ocean Engineering 156, 38-60.

Li, Y., 2019. Fully nonlinear analysis of second-order gap resonance between two floating barges. Engineering Analysis with Boundary Elements 106, 1-19.

Li, Y., Zhang, C., 2016. Analysis of wave resonance in gap between two heaving barges. Ocean Engineering 117, 210-220.

Lu, L., Teng, B., Cheng, L., Sun, L., Chen, X., 2011a. Modelling of multi-bodies in close proximity under water waves—Fluid resonance in narrow gaps. Science China Physics, Mechanics and Astronomy 54 (1), 16-25.

Lu, L., Teng, B., Sun, L., Chen, B., 2011b. Modelling of multi-bodies in close proximity under water waves—Fluid forces on floating bodies. Ocean Engineering 38 (13), 1403-1416.

Miao, G., Saitoh, T., Ishida, H., 2001. Water wave interaction of twin large scale caissons with a small gap between. Coastal Engineering Journal 43 (1), 39-58.

Molin, B., 2001. On the piston and sloshing modes in moonpools. Journal of Fluid Mechanics 430, 27-50.

Moradi, N., Zhou, T., Cheng, L., 2015. Effect of inlet configuration on wave resonance in the narrow gap of two fixed bodies in close proximity. Ocean Engineering 103, 88-102.

Newman, J.N., 2004. Progress in wave load computations on offshore structures (Invited lecture), The 23th Conference on Offshore Mechanics and Arctic Engineering (OMAE2004), New York, USA.

Ning, D., Su, X., Zhao, M., Teng, B., 2015. Numerical study of resonance induced by wave action on multiple rectangular boxes with narrow gaps. Acta Oceanologica Sinica 34 (5), 92-102.

Ning, D., Zhu, Y., Zhang, C., Zhao, M., 2018. Experimental and numerical study on wave response at the gap between two barges of different draughts. Applied Ocean Research 77, 14-25.

Pauw, W.H., Huijsmans, R.H.M., Voogt, A., 2007. Advances in the Hydrodynamics of Side-by-Side Moored Vessels, Proceedings of the 26th International Conference on Offshore Mechanics and Arctic Engineering, San Diego, California, USA. Paper No. OMAE2007-29374.

Rodríguez, M., Spinneken, J., 2016. A laboratory study on the loading and motion of a heaving box. Journal of Fluids and Structures 64, 107-126.

Saitoh, T., Miao, G., Ishida, H., 2006. Theoretical analysis on appearance condition of fluid resonance in a narrow gap between two modules of very large floating structure, Proceedings of the 3rd Asia-Pacific Workshop on Marine Hydrodynamics, Shanghai, China, pp. 170-175.

Sun, L., Taylor, R.E., Taylor, P.H., 2010. First- and second-order analysis of resonant waves between adjacent barges. Journal of Fluids and Structures 26 (6), 954-978.

Tan, L., Lu, L., Liu, Y., Sabodash, O.A., Teng, B., 2014. Dissipative Effects of Resonant Waves in Confined Space Formed by Floating Box in Front of Vertical Wall, Proceedings of the Eleventh ISOPE Pacific/Asia Offshore Mechanics Symposium, Shanghai, China. Paper No. ISOPE-P-14-080.

Tan, L., Lu, L., Tang, G.Q., Cheng, L., Chen, X.B., 2019. A viscous damping model for piston mode resonance. Journal of Fluid Mechanics 871, 510-533.

Zhao, W., Pan, Z., Lin, F., Li, B., Taylor, P.H., Efthymiou, M., 2018. Estimation of gap resonance relevant to side-by-side offloading. Ocean Engineering 153, 1-9.

Zhao, W., Wolgamot, H.A., Taylor, P.H., Taylor, R.E., 2017. Gap resonance and higher harmonics driven by focused transient wave groups. Journal of Fluid Mechanics 812, 905-939.